Research Article | Vol. 1, No. 3 | 15 Nov 2018 | OSA CONTINUUM 1068
OSA CONTINUUM

Circular intensity differential scattering (CIDS) scanning microscopy to image chromatin-DNA nuclear organization

AYMERIC LE GRATIET,[1,3] LUCA PESCE,[1,2] MICHELE ONETO,[1] RICCARDO MARONGIU,[1,2] GIULIA ZANINI,[1,2] PAOLO BIANCHINI,[1] AND ALBERTO DIASPRO[1,2,*]

[1]*Nanoscopy and NIC@IIT, Istituto Italiano di Tecnologia, Via Morego 30, 16163 Genoa, Italy*
[2]*Department of Physics, University of Genoa, Via Dodecaneso 33, 16146 Genoa, Italy*
[3]*aymeric.legratiet@iit.it*
**alberto.diaspro@iit.it*

Abstract: Circular dichroism imaging has proved a powerful and simple method for extracting information on chiral molecules without specific fluorescent labels. Numerous mathematical models show that outside the absorption band, the circular dichroism signal comes from the scattering interaction and brings additional information about the organization of biopolymers. With this article, we propose a fast method to control the polarization states without moving parts, by means of a photoelastic modulator. We implemented the technique on a modified commercial confocal microscope realizing a multimodal configuration. We demonstrate its imaging capabilities by studying the organization of chromatin DNA inside isolated cell nuclei.

1. Introduction

Optical scanning microscopy techniques based on the polarization control of the light are powerful label-free methods capable of extracting supplementary information from a medium, which has shown numerous applications for biomedical studies such as early cancer diagnosis [1,2] and ophthalmology [3,4]. Among these techniques, it was shown that Circular Dichroism (CD) microscopy gives access to the structural organization and concentration of chiral molecules in a sample [5,6]. This technique consists in detecting the difference in intensities between left and right polarization states upon the interaction with the sample. It is worth noting that the sum of such two components, i.e. the total CD signal, comes mainly from absorption and from a weak scattering component [7–10]. Outside the absorption band, the scattering variant of CD is named Circular Intensity Differential Scattering (CIDS), which is described by the following equation:

$$CIDS = \frac{I_L - I_R}{I_L + I_R} \tag{1}$$

where I_L and I_R are the detected intensities for the left and right circular polarization states, respectively. Experimental CIDS setups are very similar to each other and are based on the use of Pockels cell or photo-elastic modulator (PEM) to modulate the polarization states at a high-speed rate [11], compatible to the pixel-dwell time of any scanning microscope system [12]. However, some articles referred that PEM is more robust to thermal deviation, more compact and of easy handling [13]. If this device is coupled with a demodulation detection scheme using a Lock-in Amplifier (LA) at the reference frequency of the PEM, it is possible to analyze the difference of intensities between the right and left circular polarization states in few microseconds. Early results concerning the study of the CIDS contrast pointed out that

#341810 https://doi.org/10.1364/OSAC.1.001068
Journal © 2018 Received 8 Aug 2018; revised 5 Oct 2018; accepted 15 Oct 2018; published 13 Nov 2018

OSA CONTINUUM

this signal is strongly dependent on the chiral organization, which is valuable to obtain additional information at the molecular level. Of particular interest are the case studies about biopolymers organization such as the high-order chromatin structure in function of scattering angle [14,15] and wavelength [16,17]. Some early works proposed to develop an imaging system to extract as many information as possible from the interaction between polarized light and matter [18,19]. Some of the solutions suggested revealing the presence of chromatin DNA into cellular nuclei [20] to identify the structural orientation in biological samples [21] or to study nano-biopolymers aggregation [22]. However, most of the recent works reporting CIDS scanning or wide-field microscopy are mainly focused on the study of the molecular organization of thin layers [23,24] or metamaterials [25].

In this article, for the first time, we propose a PEM-based multimodal CIDS and confocal laser scanning microscope, applied to the study of the spatial organization of chromatin-DNA in isolated nuclei. We show that it is possible to study this bio-macromolecule outside the absorption band to improve the sensitivity of the CIDS signal from a chiral structure at the single cellular level. Furthermore, we labeled the nuclei with Hoechst 33342 to have a landmark reference for the distribution of chromatin DNA in the nucleus.

2. Materials and methods

2.1 Experimental setup

A block diagram of the experimental setup is presented Fig. 1. A commercial Nikon scanning microscope has been modified by adding a fast polarization state generator (PSG) based on a PEM and a customized transmission detection module that allows extracting the CIDS contrast pixel by pixel. The light source we used for illumination is a Ti:Sa femtosecond laser (Chameleon Ultra II Coherent Inc., Santa Clara, CA, USA), tuned at 740 nm, a wavelength outside the absorption band of biological samples. To generate the polarization states, we placed a linear polarizer at –45° reference angle and a 50 kHz PEM (PEM-100, Hinds Instruments Inc, Hillsboro, OR, USA) oriented at 0° before the objective lens [15]. The PEM modulates the polarization of the light at a resonant frequency of 50 kHz.

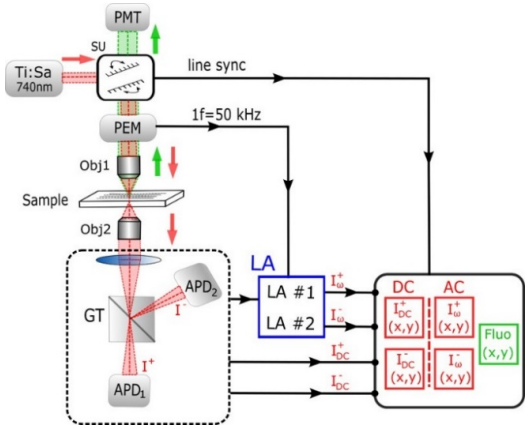

Fig. 1. Block diagram of the CIDS scanning microscope. Ti:Sa: Titanium-Sapphire coherent laser source tuned at 740 nm. SU: Scanning Unit. PEM: Photoelastic Modulator at 50 kHz resonant frequency. Obj1: Microscope objective to image the sample. Obj2: Microscope objective used as a condenser to collect the transmitted light. GT: Glan-Taylor prism. APD1 and APD2: Avalanche Photodiode for + 45° and –45° polarization detection after the GT. LA: Lock-in Amplifiers. LA#1 and LA#2: input channels of the LA, locked at 50 kHz from the reference signal of the PEM. The two APDs are both connected to each channel of the LA and also directly to the control unit. The terms " I^+ " and " I^- " are the detected intensities + 45° and –45° polarization projections after the GT, respectively. The red and green color optical path correspond to the transmitted polarimetric and to the reflected fluorescence path, respectively.

OSA CONTINUUM

Using Mueller formalism [7,26], the polarization state of the light after the sample is described with the output Stokes vector $\vec{S}_{out}$:

$$\vec{S}_{out} = \left[M_{sample}\right].\cdot\left[M_{PEM}\right].\begin{pmatrix}1\\0\\-1\\0\end{pmatrix} \tag{2}$$

where $\left[M_{sample}\right]$ and $\left[M_{PEM}\right]$ are the Mueller matrix of the sample and of the PEM respectively, which can be written as

$$\left[M_{sample}\right] = \begin{bmatrix} m_{00} & m_{01} & m_{02} & m_{03} \\ m_{10} & m_{11} & m_{12} & m_{13} \\ m_{20} & m_{21} & m_{22} & m_{23} \\ m_{30} & m_{31} & m_{32} & m_{33} \end{bmatrix} \tag{3}$$

$$\left[M_{PEM}\right] = \begin{bmatrix} 1 & 0 & 0 & 0 \\ 0 & 1 & 0 & 0 \\ 0 & 0 & \cos(\delta) & \sin(\delta) \\ 0 & 0 & -\sin(\delta) & \cos(\delta) \end{bmatrix} \tag{4}$$

In our case, the Mueller matrix of the PEM is similar to the one from a birefringent plate oriented at 0° with the time dependent retardance $\delta(t) = A\cdot\cos(\omega t)$ where A is the retardation amplitude and $\omega/2\pi = 50kHz$ is the polarization modulation frequency of the PEM.

In the case of an ideal optical alignment, after interaction with the sample, the Stokes vector is:

$$\vec{S}_{out} = \begin{pmatrix} m_{00} - m_{02}\cdot\cos(\delta) + m_{03}\cdot\sin(\delta) \\ m_{10} - m_{12}\cdot\cos(\delta) + m_{13}\cdot\sin(\delta) \\ m_{20} - m_{22}\cdot\cos(\delta) + m_{23}\cdot\sin(\delta) \\ m_{00} - m_{32}\cdot\cos(\delta) + m_{33}\cdot\sin(\delta) \end{pmatrix} \tag{5}$$

The method in our experiment consists in placing a Glan-Taylor prism oriented at + 45° after the sample to be able to select the needed Mueller-matrix coefficients as fast as possible. This optical device splits the beam in two directions with two orthogonal polarization states, which are + 45° and –45° according to the incident reference polarization states before the PEM. In terms of Mueller-matrix formalism, it consists of multiplying $\vec{S}_{out}$ by the projection Stokes vectors (1,0,1,0) or (1,0,-1,0), corresponding to the + 45° and –45° output polarization states, respectively. Using Bessel function developments at first order, the output intensity $I(t)$ measured by each detectors can be written as a modulated signal in the following way:

$$I(t) = I_{DC} + I_{\omega}\cdot\cos(\omega t) \tag{6}$$

where I_{DC} is the DC intensity of the modulated signal and I_{ω} is the modulation intensity at 50 kHz. The intensities I^{+} and I^{-} detected by the two identical detectors at + 45° and –45° are written as functions proportional to the Mueller-matrix coefficients after simplifications and are summarized in Table 1.

OSA CONTINUUM

Table 1. Expression of the modulation intensities detected at + 45° (I^+) and –45° (I^-) after the Glan-Taylor prism.

	I^+	I^-
I_{DC}	$m_{00} + m_{02}$	$m_{00} - m_{02}$
I_{ω}	$m_{03} + m_{23}$	$m_{03} - m_{23}$

In this article, we focus our study only on the CIDS contrast from the sample. From Table 1, the m_{00} and the m_{03} elements, i.e. the total transmitted light and the CIDS signal are deduced by adding the two orthogonal DC and 50 kHz measurable intensities, respectively.

We used a 100X/1.3NA Nikon objective (Plan Fluor DIC H, Nikon Instruments, Yokohama, JP) to focus the light on the sample with a diffraction-limited lateral resolution of $\approx\lambda/2NA \approx 0.3\mu m$. The light is collected using a 40X/0.6NA Nikon objective (Plan Fluor ELWD, Nikon Instruments, Yokohama, JP) as a condenser. A 50 mm focal length lens was placed between the condenser and the two detectors to maximize the field of view. A Glan-Taylor (GT10-A calcite polarizers Thorlabs, Inc., USA) prism splits the beam in two directions depending on its orthogonal polarization states. We acquired the two signals simultaneously with two identical avalanche photodiodes (APD1 and APD2 in Fig. 1) with switchable gain (PDA36A-EC Thorlabs, Inc., USA), each one connected to the same LA (HF2LI Zurich Instruments AG, SUI). The two demodulated signals were synchronously collected by the four-channel Nikon control unit (C2 + , Nikon Instruments, Yokohama, JP). At the same scanning time, the control unit also acquires the two DC signals by directly connecting the outputs of each APD to the two other channels. The conventional confocal fluorescence was collected at wavelength below 680 nm in the backward direction by switching one channel of the unit and without moving the sample.

Finally, this setup presents a multimodal scanning microscope, which couples fluorescence and the four transmission polarized channels, detected at two different wavelengths (below 680 nm for the fluorescence and 740 nm for the CIDS signal). We used Nis-Element software (Nikon Instruments, Yokohama, JP) to acquire the image and FIJI [27] to analyze the final CIDS image.

2.2 Image acquisition, calibration, and intensities

The image size is 512 × 512 pixels over a field of view (FOV) of 25 × 25 μm^2. The pixel dwell time depends on the LA integration time and we set both at 20 μs. To improve the signal-to-noise ratio, we performed frame averaging 4 times. Therefore, the acquisition of a single image takes around 20 seconds. This acquisition time is compatible with the biological temporal process of the fixed samples used in this paper. It can be reduce by decreasing the definition of the image and/or the signal-to-noise ratio, which is possible to reach an image acquisition time of 5 seconds.

To take into account the different sensitivities and gains of the two APDs and of the LA channels, we take a background image for calibration, which consists in imaging an area of the sample, which does not contain any cells. After that, the average intensity value is calculated for the two orthogonal images to obtain a rescale factor between the two APDs given by the ratio of such values and denoted as G. The background difference image between the two channels is then applied to all the raw images. An example of the calibration background image is given Fig. 2.

OSA CONTINUUM

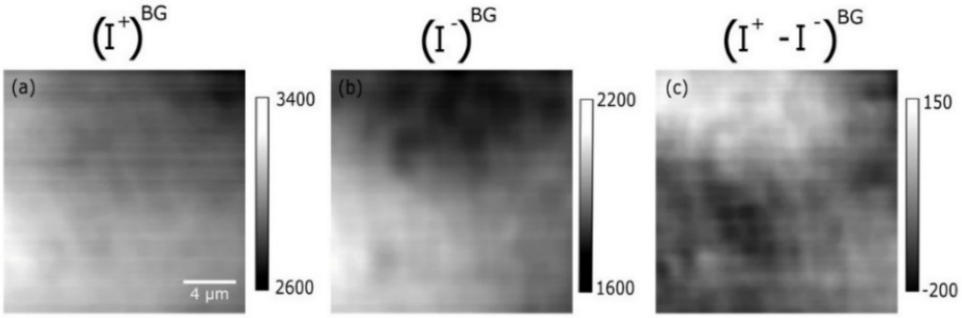

Fig. 2. Raw images corresponding of the detected signal background ("BG") image for (a) I^+ and (b) I^-. (c) The signal difference between the two channels $I^+ - I^-$. Here G, the rescale factor between the two detectors is equal to 1.6.

This background calibration step takes into account also optical systematic errors induced mainly by (1) a misalignment of the fast axis orientation of the PEM and GT referred to the input linear polarization, (2) the reflection on the glass interface of the sample, and (3) the presence of residual biological material. In the scanning configuration, additional systematic errors come from the loss of the linear polarization in all the field of view following the Fresnel laws. To compensate this loss, the field of view is reduce 6 to 10 times using the zoom function from the Nis Element software. As shown in Fig. 1, we denote I^+_{DC} and I^-_{DC}, the DC components, as well as I^+_ω and I^-_ω, the 50 kHz demodulated intensities, both measured at + 45° and –45°, respectively. To correct the difference of brightness of the final image CIDS(x,y), we apply the following operation pixel by pixel:

$$CIDS(x,y) = \frac{I^+_\omega(x,y) + G.I^-_\omega(x,y)}{I^+_{DC}(x,y) + G.I^-_{DC}(x,y)} = \frac{m_{03}(x,y)}{m_{00}(x,y)} \tag{7}$$

This equation shows that we normalize the m_{03} by the m_{00} image, which means that the CIDS(x,y) image corresponds to the ratio of the CIDS and the total transmitted light detected, that allows to have comparable and reproducible data for all the samples.

2.3 Sample preparation

For these experiments, Hek 293 cells are grown in DMEM medium supplemented with 10% FBS, 1% penicillin – streptomycin, 1% glutamine. We obtain the isolation of nuclei by using a hypotonic buffer (10 mM Hepes pH 7.5, $MgCl_2$ 2 mM, KCl 25 mM, 1 mM PMSF, 1 mM DTT and Halt protease inhibitor cocktail from Thermo Fisher Scientific, Waltham, Massachusetts, USA) for 30 min in ice, which swells the cells. Then, the cells can be easily lysed with a glass Dounce pestle with a clearance range of 0.025-0.076 mm (Technovetro s.r.l. Monza, Italy). While monitoring the cell lysis through a bright field microscope, sucrose at final concentration of 250 mM is added to the nuclei solution and the samples are centrifuged at 1200g for 10 min. The isolated nuclei are collected on pellet and are re-suspended in nuclear buffer (10 mM Hepes pH 7.5, $MgCl_2$ 2 mM, KCl 25 mM, 250 mM sucrose and Halt protease inhibitor cocktail). Then, the nuclei are centrifugated at 800g for 15 min and re-suspended in the nuclear buffer for the three times before incubation with Hoechst 33342 (Thermo Fisher Scientific) at the dilution 1:1000, for 10 min. Finally, the extracted nuclei are resuspended in a fixation solution consisting in 3.2% Paraformaldehyde (PFA) and 0.1% Glutaraldehyde (GA) in PBS. For fluorescence and CIDS scanning microscopy, the labelled nuclei are seeded on a 24 mm coverglass, previously treated with Poli-L-Lysine (Sigma-Aldrich) for 30 min at 37° C.

OSA CONTINUUM

3. Results and discussions

For several cellular phases, we expect to see a strong contrast in the CIDS signal inside the nucleus induced by the presence of chromatin DNA. However, it is worth noting that the chromatin is more compact at the nuclear periphery, in correspondence to a transcriptionally inactive region, called heterochromatin. In the deeper part of the nucleus, chromatin DNA can be dispersed, depending on the gene expression, called euchromatin [28,29]. One should note that the smaller chiral group possible to detect with this method was discussed by C. Bustamante et al. [8] and in many other early works [15]. It was shown that the CIDS signal could be sensitive to a long-range organization of chiral structures, greater than 20 nm. This scale corresponds to the spatial conformation of chromatin-DNA for the actual cell phase under study. Thus, this technique is suitable to be able to distinguish, in a specific way, the difference of compaction inside the nucleus compare to the fluorescence modality. These orders of magnitude, linked to the spatial resolution this technique can reach, give a good approximation to interpret the information brings from the CIDS images analysis, but can change by modifying the numerical aperture objective or the detection system.

Figure 3 shows the first images obtained with our CIDS scanning microscope presented in Fig. 1. Figures 3(a), 3(b), and 3(c) are the raw images $I_{\omega}^{+}(x,y)$, $I_{\omega}^{-}(x,y)$ and the CIDS image, i.e. $m_{03}(x,y)$, respectively. Figures 3(d), 3(e), and 3(f) are $I_{DC}^{+}(x,y)$, $I_{DC}^{-}(x,y)$ and the total transmitted light, i.e. $m_{00}(x,y)$ respectively. These six raw data images are enough to highlight the difference of organization into the nucleus without using fluorescent labels and without any data processing. The color scale bars help quantifying the polarimetric signal amplitude to distinguish the difference of compaction of the chromatin-DNA inside the nucleus. The contrast obtained by summarizing the two channels and presented in Figs. 3(c) and 3(f) expresses the CIDS signal and the total transmitted intensity, respectively, bringing another different contrast mechanism from the raw images [Figs. 3(a), 3(b), 3(d) and 3(e)]. The CIDS contrast in Fig. 3(c) presents different physical phenomena measured by our setup and can be explained with (1) the different compactness of chromatin-DNA, (2) the different structural organization of the biological materials and (3) the natural proteins in the biological medium.

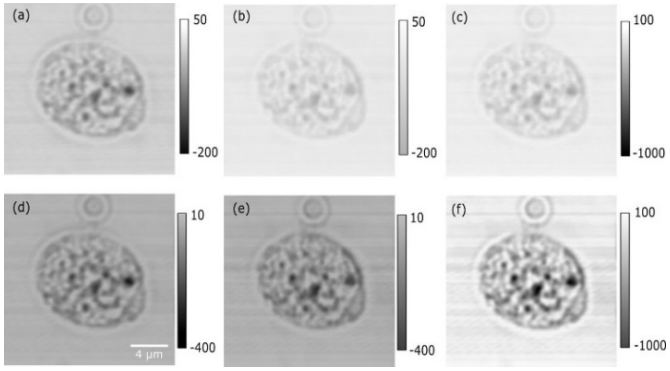

Fig. 3. (Top) Raw images of the isolated nucleus after extraction corresponding to the detected 50 kHz signals for (a) I_{ω}^{+}, (b) I_{ω}^{-} and (c) the sum of the images (a) and (b), i.e. $m_{03} = I_{\omega}^{+} + G \cdot I_{\omega}^{-}$, where G is the rescale factor between the two detectors. (Bottom) Raw images corresponding of the detected DC components signal for (d) I_{DC}^{+}, (e) I_{DC}^{-} and (f) the sum of the images (d) and (e), i.e. $m_{00} = I_{DC}^{+} + G \cdot I_{DC}^{-}$.

Figure 4 presents the superposition of the two optical microscopy modalities polarimetric and fluorescence available at the same time in our setup, without moving the sample. Indeed,

OSA CONTINUUM

to observe the different spatial organization of chromatin DNA into the nucleus, the sample is labelled using Hoechst 33342 which has a fluorescent spectrum between 510 nm and 540 nm and reveals the presence of DNA only inside the nucleus. The images in Figs. 4(a) and 4(b) show to the normalized CIDS images, i.e. the ratio between the images Figs. 3(c) and 3(f), and to the fluorescence contrast, respectively. Figure 4(c) is the merge image of Figs. 4(a) and 4(b). The intensity profile along the orange arrow in Fig. 4(c) is shown in Fig. 4(d). Blue and green plots correspond to the polarimetric [Fig. 4(a)] and the fluorescence [Fig. 4(b)] signals, respectively. Concerning the normalized CIDS image in Fig. 4(a), an important variation of intensity from the background can be observed between the nucleus and at the interface, which goes up and down in few microns, indicated by dashed bars in Fig. 4(d). As expected, the CIDS and the fluorescence images [Figs. 4(a) and 4(b)] show strong signals from the chromatin-DNA only inside the cell nucleus and nothing elsewhere. Nevertheless, a clear difference between the two modalities can be noted in term of intensity fluctuations and dynamics in the chromatin-DNA area. In principle, the optical resolution is better for fluorescence, which is proportional to I^2, contrary to the CIDS signal [15,21] limited by the Rayleigh's criterion i.e. $\approx \lambda / 2NA$. The main point is that the fluorescence emission is isotropic (i.e no preferential angular emission) and it depends only on the quantity of fluorescent molecules under illumination in the confocal volume. Thus, it is not possible to distinguish particular structures or chiral-group inside the nucleus with this imaging modality. On the other hand, CIDS emission is angular dependent [21] and it is strongly induced (1) by the chirality of the molecules, such as the radius and the pitch and (2) by the compaction of chiral-groups. Figure 4(a) demonstrates a clear proof of principle of our technique, which allows distinguishing regions with a stronger signal where the compaction is higher, i.e. heterochromatin regions, and a weaker signal, such as for the nucleoli where the compaction is lower, i.e. euchromatin region. However, the main advantage of this polarimetric method compared to the fluorescence technique is the possibility to obtain better contrast mechanisms, with no specificity on the imaging process and without using any labels. Finally, we note that biological materials can be observed around the nucleus and can induce artifacts in the polarimetric image background, which can be removed by optimizing the biological extraction protocol.

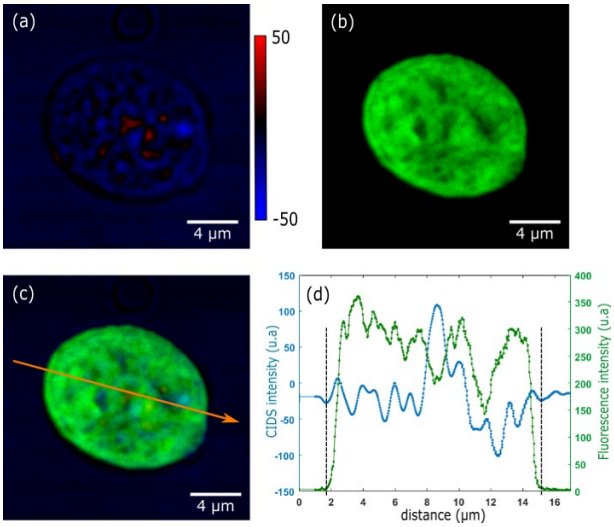

Fig. 4. (a) Normalized CIDS image of an isolated Hek nucleus after extraction. (b) Fluorescence image of the same isolated Hek nucleus labelled with Hoechst. (c) Merge of images (a) and (b). (d) Intensity plot from the orange arrow in (c). The blue plot is the intensity profile from the CIDS image (a) and the green plot is the Hoechst profile from image 4.(b). The dashed lines indicate the estimated area of the nucleus.

OSA CONTINUUM

4. Conclusion

In this article, we have reported an imaging technique for isolated nuclei using polarimetric measurements, based on the CIDS signals analysis. We believe that this method will open new way to study the mechanisms of nuclear organization and could pave the way for other applications. This microscopy technique could be a tool for the quantification of the CIDS signal to distinguish healthy from diseased cells or tissues. However, by switching the reference signal of the PEM at the first harmonic, i.e. 100 kHz, we can be also able to extract other Mueller-matrix elements, such as the linear dichroism, that can be another source of contrast for oriented biopolymers or fibers to understand for instance the orientation of proteins at this microscopic level. As preliminary results, Figs. 5 and 6 show the complete set of Mueller-matrix images available with the actual setup configuration (i.e. m_{00}, m_{02}, m_{03}, m_{22} and m_{23}).

Appendix: Other Mueller-matrix coefficients

As a proof of principle of the potentiality of this method, preliminary results are proposed by measuring all the Mueller-matrix elements available in this configuration without moving parts.

Figure 5 presents the five Mueller-matrix elements images of the same sample presented in Figs. 3 and 4, i.e. m_{00}, m_{02}, m_{03}, m_{22} and m_{23}. The coefficients m_{03} and m_{23} are extracted by summing and subtracting the two orthogonal intensity images locked at 50 kHz, respectively. By directly switching the reference signal of the PEM to 100 kHz, we can extract the coefficients m_{02} and m_{22} by summing and subtracting the two orthogonal intensity images, without moving the sample. It can be observed that some coefficients for this sample are less relevant, such as m_{23} and m_{02}. Indeed, some specific polarization interactions are not sensitive to the structures, the orientation and the thickness of the nucleus. The image m_{22} is linked to the total transmitted light, which explains the strong contrast correlated to the m_{00} image.

Figure 6 presents the images in Fig. 5, normalized by the total transmitted light, i.e. the m_{00} image. We can observe variabilities in terms of the dynamic range as a function of the Mueller-coefficients presented by the chromatin-DNA organization. In this way, the number of information available with this technique is interesting to quantify and compare the different polarization effects of this kind of sample. Indeed, common spectrometric measurements for biopolymers are used to measure only few bio-molecules in a small volume at specific polarization states. Using scanning microscopy in the 2D focal plane, we can have access to information from a complex biological system under illumination, sensitive to all the polarization states in a short time. By analyzing Mueller-matrix element-by-element, it is possible to discriminate all the effects present in the image and to quantify the amplitude of the polarimetric effects, such as linear or circular dichroism and birefringence. By selecting few elements, some information about the scattering is also available.

OSA CONTINUUM

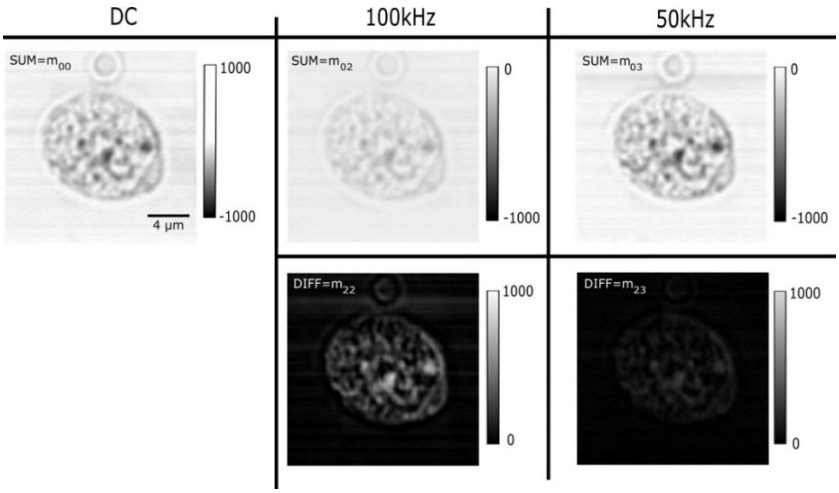

Fig. 5. Mueller-matrix element images of an isolated Hek nucleus after extraction. The Mueller-matrix coefficients are available without moving parts and are obtained by comparing the raw data images, shown in Fig. 2. "SUM" and "DIFF" correspond to the sum and the difference of the two channels for both 50 kHz and 100 kHz reference signal of the PEM.

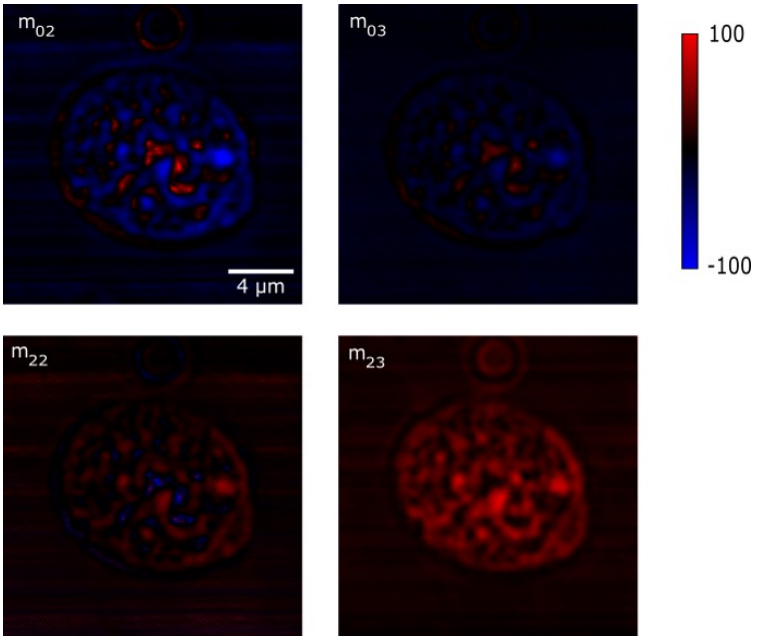

Fig. 6. Normalized Mueller-matrix element images of an isolated Hek nucleus after extraction, available for the actual experimental configuration of the microscope.

It can be noted that the membrane signal is lost with some Mueller-matrix coefficients, contrary to the chromatin-DNA, whose signal is stronger and which shows an interesting intensity dynamic range. Considering that some Mueller-matrix elements have an angular dependence, the membrane signal is probably not collected in the forward direction by the condenser, in this setup configuration. Considering that angular detection systems coupled with a microscopy technique are difficult to be implemented and can be expensive, we can use some elements as a promising tool to remove artifacts from the image of the sample or just to select the signal we are interested in, in an easy and cheap way.

OSA CONTINUUM

Funding

Fondazione Istituto Italiano di Tecnologia (I.I.T., Genoa, Italy).

Acknowledgment

We thank the Nikon Imaging Center at the Fondazione Istituto Italiano di Tecnologia (Genoa, Italy) for the support in the realization of the experiment.

References

1. N. Mazumder, J. Qiu, F. J. Kao, and A. Diaspro, "Mueller matrix signature in advanced fluorescence microscopy imaging," J. Opt. **19**(2), 025301 (2017).
2. A. Le Gratiet, M. Dubreuil, S. Rivet, and Y. Le Grand, "Scanning Mueller polarimetric microscopy," Opt. Lett. **41**(18), 4336–4339 (2016).
3. J. M. Bueno and M. C. Campbell, "Confocal scanning laser ophthalmoscopy improvement by use of Mueller-matrix polarimetry," Opt. Lett. **27**(10), 830–832 (2002).
4. K. M. Twietmeyer, R. A. Chipman, A. E. Elsner, Y. Zhao, and D. VanNasdale, "Mueller matrix retinal imager with optimized polarization conditions," Opt. Express **16**(26), 21339–21354 (2008).
5. L. A. Nafie, "Circular polarization spectroscopy of chiral molecules," J. Mol. Struct. **347**, 83–100 (1995).
6. K. Claborn, E. Puklin-Faucher, M. Kurimoto, W. Kaminsky, and B. Kahr, "Circular dichroism imaging microscopy: application to enantiomorphous twinning in biaxial crystals of 1,8-dihydroxyanthraquinone," J. Am. Chem. Soc. **125**(48), 14825–14831 (2003).
7. C. F. Bohren and D. R. Huffman, *Absorption and Scattering of Light by Small Particles* (Wiley, 1983).
8. C. J. Bustamante, "Circular Intensity Differential Scattering of chiral molecules," Ph. D Thesis California Univ., Berkeley (1980).
9. C. Bustamante, I. Tinoco, Jr., and M. F. Maestre, "Circular differential scattering can be an important part of the circular dichroism of macromolecules," Proc. Natl. Acad. Sci. U.S.A. **80**(12), 3568–3572 (1983).
10. D. Keller, C. Bustamante, M. F. Maestre, and I. Tinoco, Jr., "Imaging of optically active biological structures by use of circularly polarized light," Proc. Natl. Acad. Sci. U.S.A. **82**(2), 401–405 (1985).
11. J. C. Kemp, "Piezo-optical birefringence modulators: new use for a long-know effect," J. Opt. Soc. Am. **59**(8), 950–954 (1969).
12. S. Alali, A. Gribble, and I. A. Vitkin, "Rapid wide-field Mueller matrix polarimetry imaging based on four photoelastic modulators with no moving parts," Opt. Lett. **41**(5), 1038–1041 (2016).
13. E. Huber, N. Baltzer, and M. von Allmen, "Polarization modulation ellipsometry: a compact and easy handling instrument," Rev. Sci. Instrum. **56**(12), 2222–2227 (1985).
14. K. S. Wells, D. A. Beach, D. Keller, and C. Bustamante, "An analysis of circular intensity differential scattering measurements: studies on the sperm cell of eledone cirrhosa," Biopolymers **25**(11), 2043–2064 (1986).
15. A. Diaspro, M. Bertolotto, L. Vergani, and C. Nicolini, "Polarized light scattering of nucleosomes and polynucleosomes-in situ and in vitro studies," IEEE Trans. Biomed. Eng. **38**(7), 670–678 (1991).
16. M. F. Maestre, G. C. Salzman, R. A. Tobey, and C. Bustamante, "Circular dichroism studies on single chinese hamster cells," Biochemistry **24**(19), 5152–5157 (1985).
17. F. Livolant, W. Mickols, and M. F. Maestre, "Differential polarization microscopy (CD and linear dichroism) of polytene chromosomes and nucleoli from the dipteran sarcophaga footpad," Biopolymers **27**(11), 1761–1769 (1988).
18. M. Kim, D. Keller, and C. Bustamante, "Differential polarization imaging. I. theory," Biophys. J. **52**(6), 911–927 (1987).
19. W. C. Mickols, C. Bustamante, M. F. Maestre, I. Tinoco, and S. H. Embury, "Differential polarization microscopy: a new imaging technique," Biotechnology **3**(8), 711–714 (1985).
20. W. Mickols and M. F. Maestre, "Scanning differential polarization microscope: its use to image linear and circular differential scattering," Rev. Sci. Instrum. **59**(6), 867–872 (1988).
21. L. Finzi, L. Ulibarri, and C. Bustamante, "Differential polarization imaging. V. numerical aperture effects and the contribution of preferential scattering and absorption to the circular dichroism images," Biophys. J. **59**(6), 1183–1193 (1991).
22. V. K. Gupta and J. A. Kornfield, "Polarization modulation laser scanning microscopy: a powerful tool to image molecular orientation and order," Rev. Sci. Instrum. **65**(9), 2823–2828 (1994).
23. F. Tantussi, F. Fuso, M. Allegrini, N. Micali, I. G. Occhiuto, L. M. Scolaro, and S. Patanè, "Linear and circular dichroism in porphyrin J-aggregates probed by polarization modulated scanning near-field optical microscopy," Nanoscale **6**(18), 10874–10878 (2014).
24. T. Yamada, H. Onuki, M. Yuri, and S. Ishizaka, "Microscopic imaging of circular dichroism using a polarizing undulator," J. Appl. Phys. **39**(1), 310–315 (2000).
25. J. H. Freudenthal, E. Hollis, and B. Kahr, "Imaging chiroptical artifacts," Chirality **21**(1E Suppl 1), E20–E27 (2009).
26. H. Mueller, "The foundations of optics," J. Opt. Soc. Am. **38**, 661–662 (1948).

OSA CONTINUUM

27. J. Schindelin, I. Arganda-Carreras, E. Frise, V. Kaynig, M. Longair, T. Pietzsch, S. Preibisch, C. Rueden, S. Saalfeld, B. Schmid, J.-Y. Tinevez, D. J. White, V. Hartenstein, K. Eliceiri, P. Tomancak, and A. Cardona, "Fiji: an open-source platform for biological-image analysis," Nat. Methods **9**(7), 676–682 (2012).
28. D. Zink, A. H. Fischer, and J. A. Nickerson, "Nuclear structure in cancer cells," Nat. Rev. Cancer **4**(9), 677–687 (2004).
29. H. D. Ou, S. Phan, T. J. Deerinck, A. Thor, M. H. Ellisman, and C. C. O'Shea, "ChromEMT: visualizing 3D chromatin structure and compaction n interphase and mitotic cells," Science **357**(6349), eaag0025 (2017).